Construction of Moiré-like lignin based carbon electrodes to efficiently improve the performance of photo-assisted supercapacitors

Wang Yizhe[1], Li Cong[1], Yuan Meng[1], Liu Xing[2], He Yanzhen[3], Guo Weimin[1], Jiao Haochen[1], Li Yudong[1,*], Yang Haiyue[1], Wang Chengyu[1,*]

(1. *Key Laboratory of Bio-based Material Science & Technology*, *Ministry of Education*, *Northeast Forestry University*, *Harbin* 150040, *China*;
2. *School of Materials Science and Engineering*, *Yancheng Institute of Technology*, *Yancheng* 224051, *China*;
3. *School of Chemical Engineering*, *Hebei University of Technology*, *Tianjin* 300130, *China*)

Abstract: Conventional lignin-based carbons typically have sluggish ion transport and a limited number of active sites, which restrict their performance as electrodes in supercapacitors. A Moiré-like morphology was engineered by the in-situ deposition of lignin carbon onto DVD matrix onto lignin carbon for the fabrication of a photo-assisted supercapacitor (PASC). The Moiré-like structure modulates light propagation across different frequencies by dispersion effects, thereby increasing surface light absorption and improving the electrochemical performance of the PASC. Under illumination, the carbon has a specific capacitance of 253.5 F g^{-1} at 0.5 A g^{-1}, corresponding to a 35.6% improvement over one without this grating surface (186.9 F g^{-1}). A symmetrical capacitor using this material has an areal capacitance of 58.84 mF cm^{-2} and an energy density of 4.46 Wh kg^{-1} at a power density of 365.2 W kg^{-1}, maintaining 85.2% of its initial capacitance after 5000 cycles, thus demonstrating excellent cycling stability. This work suggests a cost-effective strategy to simultaneously improve the light-harvesting ability and capacitive performance of PASCs.

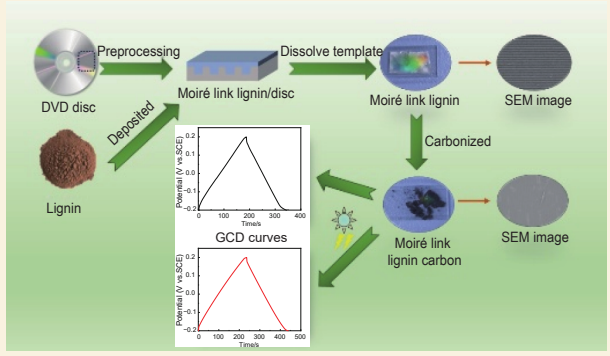

Key words: Moiré-like structure；Photo-assisted supercapacitors；Lignin carbon；Structural engineering；Light-harvesting

1 Introduction

In recent years, photo-assisted supercapacitors (PASCs) have attracted considerable attention as emerging energy storage devices because they integrate light harvesting with electrical energy storage[1–2]. Compared to conventional supercapacitors, PASCs demonstrate superior energy density, cycling stability, and charge-discharge efficiency, particularly as a result of their electro-optical energy storage synergy[3–4]. Carbon-based materials, particularly lignin-carbon electrodes, have emerged as promising candidates for PASCs due to their favorable conductivity, tunable surface chemistry, low cost and abundant availability[5–6]. However, despite their success in conventional electrochemical systems, carbon electrodes face critical challenges in PASCs, including limited photoelectric conversion efficiency, suboptimal pore architectures, and inefficient light-electricity coupling[7–9]. Lignin carbon materials are regarded as promising candidates for PASC electrodes, due to their advantageous properties, including their low production cost and good electrochemical stability. However, their performance in photo-assisted systems is often limited by structural disorder and compositional heterogeneity. The broad molecular weight distribution of lignin results in irregular pore structures after carbonization, which restrict ion diffusion and compromise the photoelectric conversion efficiency of the electrodes[10–12]. More critically, the in-

Received: January 14, 2026
Revised: March 05, 2026
Accepted: March 05, 2026

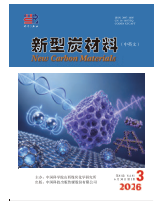

herently low electrical conductivity of lignin-based carbons poses a significant challenge, as efficient photo-to-electrical energy conversion hinges on expeditious electron transport. Despite the success of strategies such as pore structure engineering and material compositing, which have yielded improvements, there remains a challenge in the simultaneous enhancement of photoelectric conversion efficiency and electrical conductivity while preserving low cost[13–14]. This issue remains a central challenge in the development of high-performance PASC.

To address these challenges, current research focuses on three main strategies: optimizing electrode architectures to accelerate ion diffusion and photoelectric conversion, enhancing electrical conductivity by compositing and doping, and exploring synergistic photoelectric energy storage mechanisms[15–18]. Li et al.[19] adopted a "one-stone-two-birds" strategy using potassium ferrate, which simultaneously enabled activation and pore formation. The resulting carbon material demonstrated a specific surface area of 2351.6 m^2/g, a meso-porosity ratio of 25.6%, and exhibited 94% retention of its initial capacity after 20 000 cycles at a current density of 10 A/g. Ma et al.[20] prepared a sodium lignosulfonate (LS)/$Ti_3C_2T_x$ (MXene) composite electrode and enhanced its electrochemical performance by optimizing the LS/MXene mass ratio and ultrasonication time. In the experiment, the composite electrode was subjected to a mass ratio of 2∶8 and 10 min of ultrasonication. This resulted in a specific capacitance of 310 F/g at 2 mV/s and 185 F/g at 100 mV/s. Despite these advances, significant challenges remain. The hierarchical pore networks of lignin carbons have been found to be ineffective in facilitating directional ion transport. This has resulted in experimental ion diffusion coefficients that are over 60% lower than theoretical predictions for conventional tortuous pores[21–24]. Moreover, the inherently low electrical conductivity (a consequence of electron migration barriers between amorphous carbon regions and graphitic crystallites) typically remains below 10 S/m, thereby limiting the high-power performance of lignin-based carbon electrodes. Collectively, these studies demonstrate meaningful progress in improving the photoelectric performance of hierarchical porous carbon electrodes[19,25–26].

The hierarchical pore structure and low inherent conductivity of lignin carbon materials act as significant impediments to their broader use in supercapacitors. Recent studies have sought to enhance the performance of supercapacitors by controlling electrode morphology and applying external energy stimuli, including magnetic, thermal and electric fields[27–28]. Hérou et al.[29] developed freestanding electrodes from densified lignin-based carbon nanofibers. Uniaxial compression raised the electrode density sixfold, which effectively minimized inactive "dead volume" while preserving capacitive contributions from the porous structure, yielding a markedly improved volumetric energy density. Chen et al.[30] employed a stepwise dissolution-centrifugal separation strategy induced by the strong polarity of lignosulfonate. Hierarchical porous carbon with precisely tunable pore structures was obtained by a one-step carbonization process. The resulting material exhibited a high specific surface area of 1537 $m^2\ g^{-1}$ and a total pore volume of 1.33 $cm^3\ g^{-1}$, and delivered an areal capacitance of 88.1 mF cm^{-2} along with an energy density of 3.1 μWh cm^{-2} in micro-supercapacitors. Kim et al.[31] developed a reversible, photo-switchable supercapacitor using an azobenzene-functionalized polymer composite electrolyte. Evidently, under optical stimulation, the supercapacitor demonstrated a substantial capacitance modulation of 105%, accompanied by a rapid response time of approximately four minutes. While these advances introduce new approaches to improve the performance of carbon-based PASC, the development of more efficient photo-electrochemical synergy and the simultaneous enhancement of electrode stability and conductivity remain critical challenges.

A fundamental objective of this research endeavor is the integration of customized morphological frameworks with external energy sources. The overarching aim of this integration is to enhance light absorption, extend the duration of photo-responses, in-

crease the frequency of photo-reaction cycles, and improve photo-to-charge conversion efficiency in PASC. Photonic crystals and Moiré patterns are optical structures characterized by periodic geometric repetition, primarily used in optical functional components[32]. High-energy photons concentrate at submicron scales, so the characteristic dimensions of light-responsive optical structures typically range from 10 to 1000 nm[33–35]. In this range, inverse opal architectures are common but often require complex synthesis[36]. Replication methods—such as mimicking leaf surfaces or wood templates—offer a straightforward and efficient approach to fabricating micro-nano structures, gaining widespread use in functional materials[37–39]. In contrast, DVDs encode information using a Moiré-like microstructure with grooves and lands measuring 50–5000 nm wide[40]. These configurations are easily fabricated using low-power lithography on recording surfaces[41–42]. Moreover, beyond simple stripe patterns, complex morphologies such as S-curves, triangles, and circles can also be efficiently produced[43–45]. These tailored microstructures can serve as replication templates, producing Moiré-like materials with customized optical response characteristics[46–47]. According to Fermat's principle, adjusting the arrangement of multiple Moiré-like elements enables modulation of the collision, escape, and trajectory of light waves at different frequencies[48]. This provides a potential method to control the composition and efficiency of different optical frequencies during photo-reactions in supercapacitors, thus influencing photogenerated carrier populations and overall capacitive behavior[49]. Incorporating Moiré-like structures into carbon-based electrodes through morphological engineering has emerged as a promising approach for improving the performance of carbon-based PASCs.

In this study, affordable and accessible DVDs were utilized as templates to fabricate novel Moiré-patterned lignin materials using a replication technique. The high-temperature carbonization of the lignin precursor resulted in the formation of the corresponding Moiré-like lignin carbon electrode. The incorporation of a Moiré-like optical structure on the electrode surface led to a substantial enhancement in light propagation across different frequencies via dispersion effects, thereby improving the electrochemical performance of the PASC. It was demonstrated that, under illumination, the electrode exhibited enhanced capacitance at particular current densities, thereby demonstrating superior performance in comparison to equivalent electrodes that lacked the Moiré morphology. This study proposes a synergistic approach that integrates tailored morphology design with photo-assisted enhancement to improve electrode performance, thus providing a novel direction for the advancement of high-performance PASC.

2 Materials and methods

2.1 Materials

Hydrochloric acid (HCl, 36.0%–38.0%, Sinopharm Chemical Reagent Co., Ltd.), sulfuric acid (H_2SO_4, ⩾99%, Sinopharm Chemical Reagent Co., Ltd.), lignin (Daqing Shengquan Co.,Ltd.), sodium hydroxide (NaOH, Macklin), dichloromethane (CH_2Cl_2, CP grade), absolute ethanol (⩾99.7%, AR grade, Tianjin Tianli Chemical Reagent Co., Ltd.), polyvinylidene fluoride (PVDF, Beijing Inno Chem Science & Technology Co., Ltd.), N-methyl-2-pyrrolidone (NMP, AR grade, Tianjin Damao Chemical Reagent Co., Ltd.), and sodium sulfate anhydrous (Na_2SO_4, Tianjin Tianli Chemical Reagent Co., Ltd.).

2.2 Synthesis of the Moiré-like lignin carbon

A commercial DVD was divided into four equal segments, and the protective layer was removed. The segments were then subjected to a sequential rinsing process with ethanol and deionized water to eradicate surface contaminants and residual dyes. They were then subjected to ultrasonication in deionized water and ethanol for 1 h each to ensure complete dye removal from the polycarbonate layer. Subsequently, the segments were subjected to a thorough washing process with ethanol, acetone, and deionized water until they attained complete optical transparency. Thereafter, they were air-dried in a glass dish and stored for future use.

As shown in Fig. 1, lignin was dissolved in 1 mol L^{-1} NaOH solution at 1.5% mass fraction, with continuous stirring at 500 r min^{-1} for 2 h. The pre-treated disc template was immersed in the lignin solution and stirring continued for an additional 12 h to ensure uniform coating. The mixture was transferred to a petri dish and subsequently dried in an oven at 80 °C for 12 h. This process ensured the evaporation of moisture, thereby forming an M-lignin/disc template composite. After cooling, the composite was immersed in dichloromethane (CH_2Cl_2) for 72 h to completely dissolve the polycarbonate template. The resultant Moiré-patterned lignin material was rinsed with dichloromethane, ethanol, and deionized water, after which it was dried in a vacuum oven at 60 °C for 2 h.

The lignin material was carbonized in a tube furnace under nitrogen at 600, 800, 1000 and 1200 °C. The resulting products were designated as MLC-600, 800, 1000 and 1200 for subsequent analysis. Following a period of cooling to room temperature, thorough washing of the carbonized products with deionized water was carried out to eliminate any impurities. The subsequent drying of the products at 80 °C for a period of 2 h was undertaken to yield the final Moiré-like lignin carbon materials. For comparison, a reference lignin carbon material without the Moiré structure was prepared following the procedure outlined in Supplementary Information.

2.3 Characterization

A series of instrumental analyses were employed to comprehensively characterize the synthesized samples. The surface features and elemental distribution were examined using SEM (Hitachi TM 3030) equipped with an EDS detector (Oxford UltimMax 40). Crystallographic information was obtained by XRD (Shimadzu LabX XRD-6100) within a 2θ range of 10°-80°. Raman spectroscopy (inVia Qontor) was applied to probe the carbon structure, and XPS (Thermo Fisher Scientific K-Alpha) was utilized to determine the chemical states of the elements.

2.4 Fabrication and testing of the Moiré-like lignin carbon electrode

The electrochemical performance of Moiré-like lignin carbon was evaluated using a three-electrode configuration in accordance with the established standard practice. The fabrication of electrodes followed the method outlined by Cai et al.[40] A homogeneous slurry was methodically formulated by uniformly mixing the active materials (MLC-600, MLC-800, MLC-1000, MLC-1200) with conductive carbon

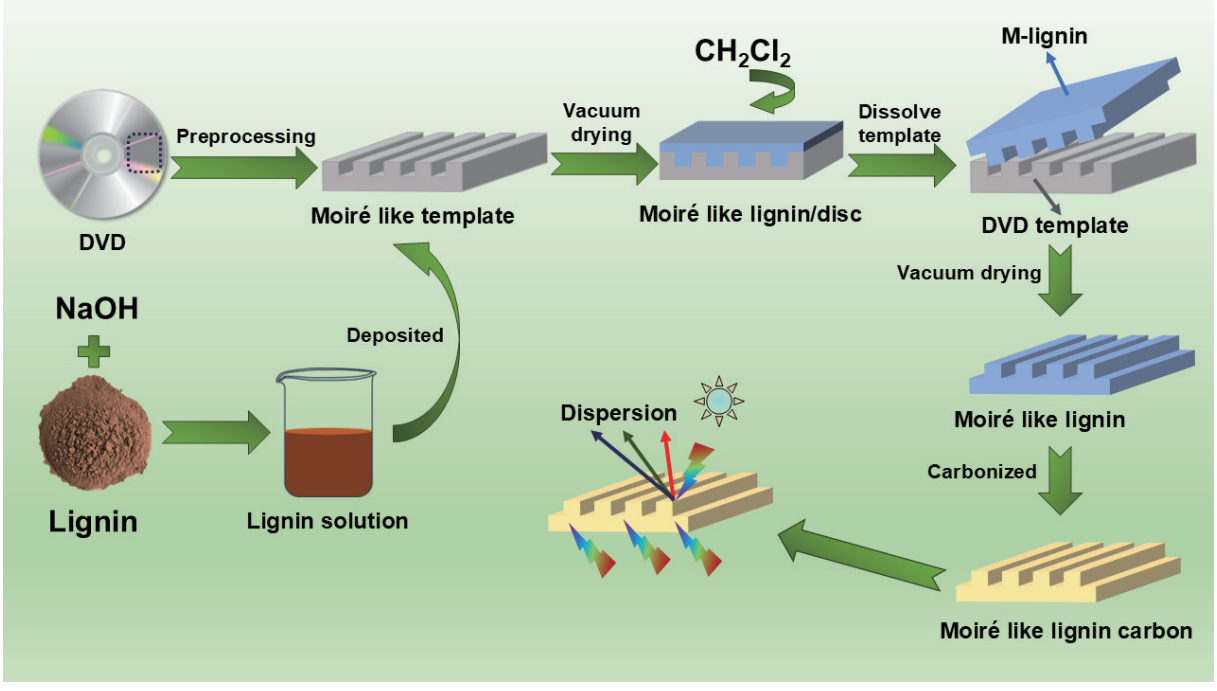

Fig. 1 Synthesis process of the Moiré-like lignin carbon

black and polyvinylidene fluoride (PVDF) binder at an 8∶1∶1 (mass ratio). N-Methyl-2-pyrrolidone (NMP) was utilized as the solvent in this synthesis. The slurry was subsequently applied to nickel foam substrates (1 cm × 2 cm) that had undergone pretreatment, thereby confining the active material to a specific area of 1 cm × 1 cm. The coated electrodes were subjected to vacuum drying at a temperature of 80 °C for a duration of 12 h. This was followed by a compression at an applied pressure of 10 MPa. The resulting electrodes possessed an active material loading of 5-6 mg.

The electrochemical configuration, schematically shown in Fig. S1, consisted of a three-electrode system employing 0.5 mol L^{-1} Na_2SO_4 as the electrolyte, a saturated calomel electrode (SCE) as the reference, and a platinum plate as the counter electrode. Prior to data acquisition, the working electrode was immersed in the electrolyte for 10 min to reach equilibrium. Electrochemical tests, including cyclic voltammetry (CV), galvanostatic charge–discharge (GCD), and electrochemical impedance spectroscopy (EIS), were conducted on a CHI 660E electrochemical workstation (Chenhua, China). The CV and GCD experiments were performed in the potential window of −0.2 to +0.2 V (vs. SCE). A 50 W xenon lamp (PLS-SXE300+, Perfectlight) provided full-spectrum visible irradiation, while EIS measurements were obtained at open-circuit potential in the frequency range of 0.01–100 kHz.

2.5 Assembly of (MLC-800 ||MLC-800) supercapacitor

The fabrication of the working electrode, schematically shown in Fig. 2, involved mixing deionized water (400 μL), isopropanol (400 μL), Nafion solution (200 μL), and 20 mg of active material, followed by ultrasonication for 1 h to form a uniform slurry. Subsequently, 100 μL of the dispersion was drop-cast onto a pre-cleaned fluorine-doped tin oxide (FTO) glass substrate (1 cm × 1 cm) and dried to obtain the working electrode. A PVA/H_2SO_4 gel served as the electrolyte, with qualitative filter paper functioning as the separator between 2 identical electrodes. All electrochemical measurements were performed under full-spectrum visible illumination provided by a 50 W xenon lamp (PL-X300D, Beijing Princeton Technology). The characterization included CV and GCD in the 0–0.8 V potential range, EIS recorded at open-circuit potential from 0.01 to 10^5 Hz, and long-term cycling stability at 5 mA cm^{-2} (Fig. S1).

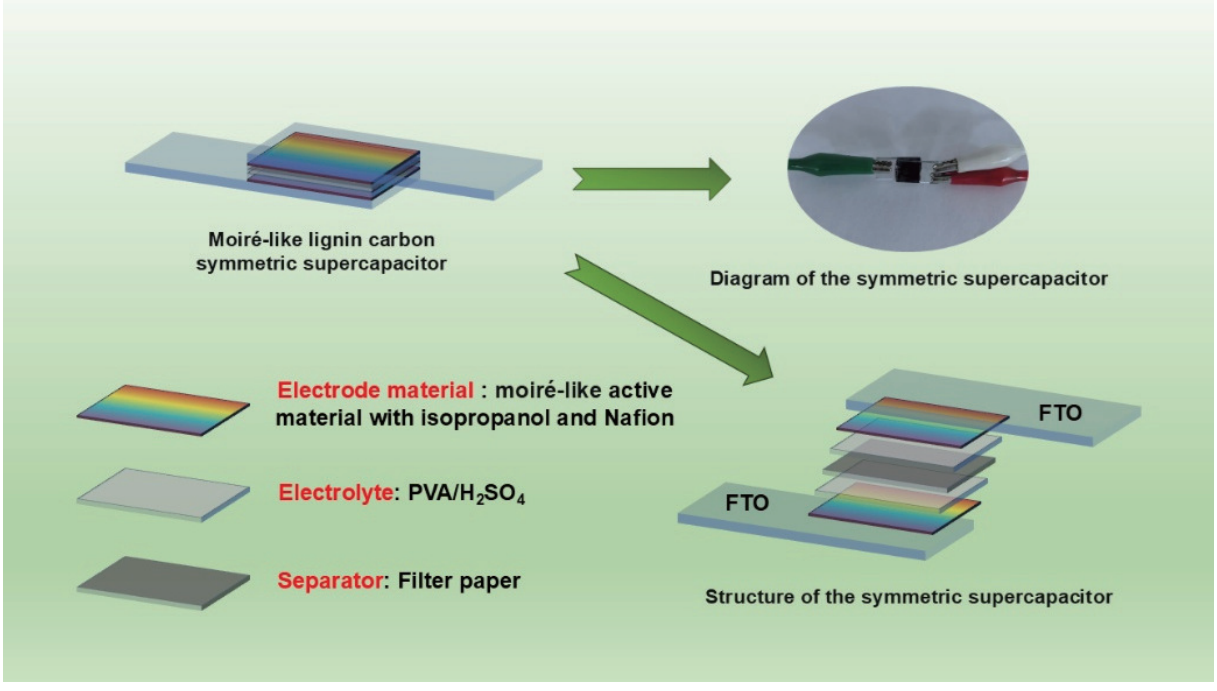

Fig. 2 Schematic diagram of the structure of a Moiré-patterned lignin-carbon symmetric supercapacitor

3 Results and discussion

3.1 Morphology

As demonstrated in Fig. 3b, the SEM image displays the fabrication of a structural template using a low-cost DVD for the production of a Moiré-like lignin sample. The surface of the material appears smooth and exhibits uniformly distributed ridge–groove features, closely matching the groove pattern of the DVD template shown in Fig. 3a. The measured stripe widths of the DVD template and the replicated Moiré-like lignin are 0.625 and 0.633 μm, respectively, confirming accurate morphological transfer from the optical disc to lignin through template replication. After carbonization at 800 °C, the MLC-800 sample retains its ridge–groove morphology (Fig. 3c), demonstrating excellent thermal stability and structural integrity of the Moiré-like architecture during carbonization. The stripe width of MLC-800 is 0.635 μm. Furthermore, SEM images of MLC-800 (Fig. S2) taken after grinding show that the material retains its characteristic stripe-groove morphology. This demonstrates that the Moiré-like structure is not destroyed during grinding. As shown in Fig. S3, digital photographs of the prepared Moiré-like lignin materials show distinct diffraction colors on both Moiré-like lignin and MLC-800 surfaces. These optical effects arise from light interference caused by incident light interacting with the periodic stripe arrangement, visually confirming the successful formation of the Moiré-like structure and demonstrating the ability of such micro–nano architectures to manipulate light propagation[48]. Incorporating Moiré-like structures into carbon materials is expected to enhance light dispersion, regulate propagation pathways and photon energy distribution, and improve electrolyte wettability and ion transport at electrode interfaces[40]. These synergistic effects are expected to enhance capacitive performance in PASC and extend their charge–discharge cycle life. Elemental mapping (EDS) of MLC-800 (Fig. 3d-f) demonstrates that the material is predominantly composed of C, N and O. The oxygen content is substantially reduced compared to uncarbonized lignin, a transformation that enhances electronic conductivity and consequently improves electrochemical performance[50].

3.2 Structure

Fig. 4a presents the XRD patterns of Moiré-like lignin carbon materials synthesized at various carbonization temperatures, along with a control sample without the Moiré-like structure. All the samples exhibited broad diffraction peaks, centred at approximately $2\theta = 23.9°$ and 43.5°, corresponding to the (002) and (100) planes of graphite, respectively. This finding indicates that a predominant amorphous carbon structure is present[51]. Among them, MLC-800 shows

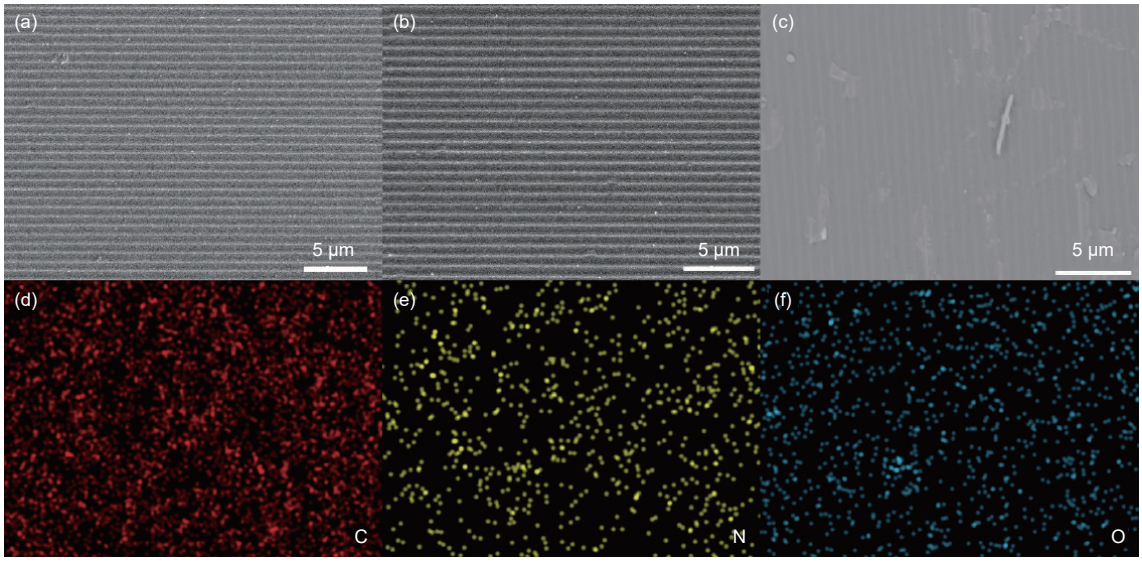

Fig. 3 SEM images of (a) DVD, (b) Moiré-like lignin and (c) Moiré-like lignin carbon. (d-f) EDS image of Moiré-like lignin carbon

the strongest diffraction peak intensity. As the carbonization temperature is elevated, there is a concomitant gradual decrease in the intensity of the characteristic peaks. This decline indicates that 800 °C is the temperature at which the highest degree of graphitic ordering is achieved under the given conditions. The reduction in graphitization at higher temperatures can be attributed to structural defects arising from the removal of heteroatoms within the lignin backbone[52]. In contrast, the sample carbonized at 600 °C exhibits significantly lower diffraction intensity, likely due to insufficient carbonization, resulting in incomplete decomposition of oxygen-containing groups and unstable carbon edges, which hinder the development of a well-ordered carbon framework. Fig. 4b displays the high-resolution C 1s XPS spectrum of MLC-800, deconvoluted into 4 distinct peaks assigned to C=C (284.0 eV), C−C (284.8 eV), C−O/C−N (286.8 eV), and C=O/C=N (288.0 eV) bonds[53–54]. Fig. 4c and 4d show the high-resolution N 1s and O 1s XPS spectra of MLC-800, respectively. The corresponding spectra reveal distinct peaks at 400.4 and 531.2 eV, confirming the presence of graphitic N and O in MLC-800. According to XPS quantitative analysis, the mass contents of N and O are 6.37% and 16.04%, respectively, reflecting the material's fundamental chemical composition. The presence of these functional groups is further confirmed by the FTIR spectrum shown in Fig. S4[55]. As shown in the XPS survey spectrum in Fig. S5, the relatively low concentration of C−O functional groups in MLC-800 enhances electrical conductivity, thereby improving the material's capacitive performance[50].

As illustrated in Fig. 4e-j, Raman spectra of lignin carbon materials vary with respect to the sintering temperature. As demonstrated in Fig. 4e, all 4 samples display distinct *D* and *G* bands at approximately 1306 and 1602 cm^{-1}, respectively, suggesting the coexistence of amorphous and graphitic domains in the Moiré-like lignin carbon. The Raman spectra were then deconvoluted into four constituent peaks, as illustrated in Fig. 4g-j. The D_1 peak, located at 1320 cm^{-1}, is indicative of disordered carbon found at the edges of graphite. The D_3 band at 1480 cm^{-1} is indicative of vibrations in amorphous sp^3-hybridised carbon[56]. The D_4 band at 1185 cm^{-1} is associated with disordered graphitic lattices, and the *G* band at 1594 cm^{-1} originates from the in-plane C−C stretching of sp^2-hybrid-

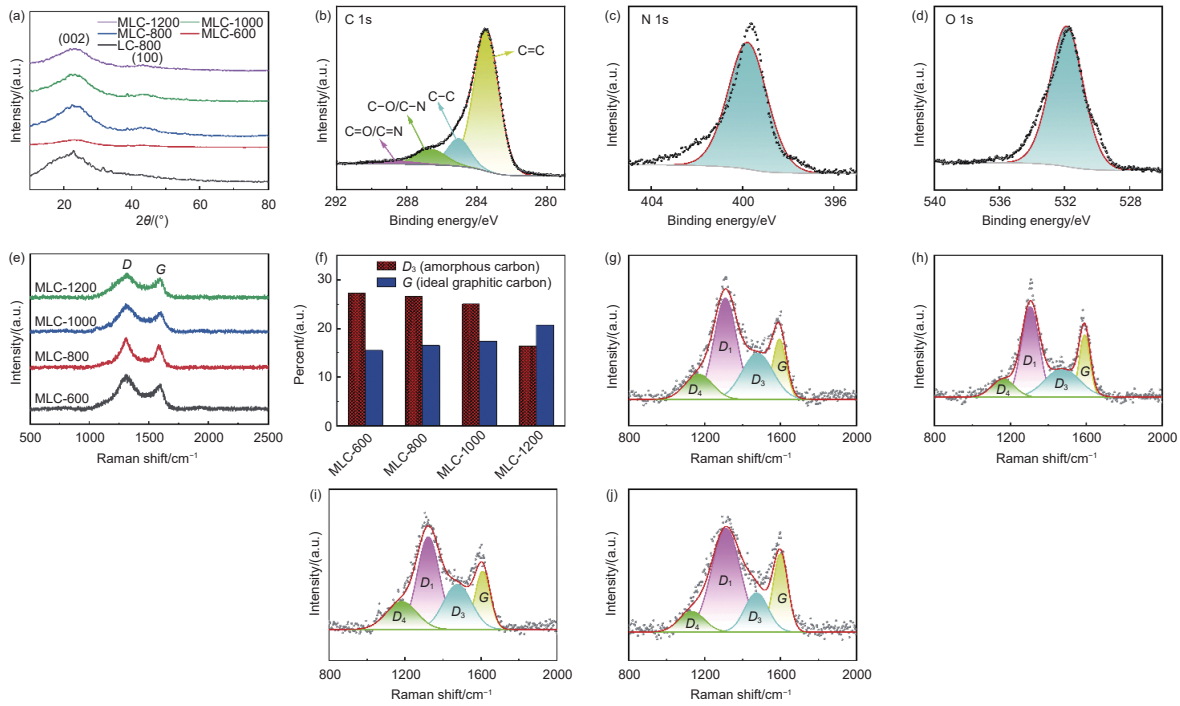

Fig. 4 (a) XRD spectra of lignin carbon. High-resolution (b) C 1s, (c) N 1s and (d) O 1s XPS spectrum of MLC-800. (e) Raman spectra of lignin carbon. (f) The proportion of lignin carbon. (g-j) Raman spectra of (g) MLC-600, (h) MLC-800, (i) MLC-1000 and (j)MLC-1200

ized graphitic carbon. With an increase in sintering temperature a decline in relative intensity of the D_3 band from 27.31% to 16.35% was observed, whilst the G band exhibits an increase from 15.42% to 20.78%, as illustrated in Fig. 4f. These trends indicate a reduction in amorphous carbon and an increase in graphitization, as evidenced by the decreasing I_{D_3}/I_G ratio[57].

3.3 Electrochemical analysis

As illustrated in Fig. 5a and 5b, the CV curves are depicted at a scan rate of 5 mV s^{-1} and the GCD curves are presented at a current density of 0.5 A g^{-1}, respectively. The CV curves of samples prepared at varying carbonization temperatures exhibit near-ideal triangular shapes, while the GCD curves retain quasi-rectangular profiles, thereby confirming the typical double-layer capacitive behavior exhibited by all materials[58–59]. As the temperature of the carbonization process is increased, the integrated CV area firstly expands and subsequently contracts, displaying a trend that is analogous to that of the GCD discharge duration. This trend indicates enhanced graphitic ordering at moderate temperatures, while excessively high temperatures lead to structural defects caused by heteroatom removal from the carbon framework. The specific capacitances, calculated using Formula S1 (Supporting Information) and applied current of 0.5 A g^{-1}, are 46.1, 186.9, 159.4 and 67.7 F g^{-1} for MLC-600, MLC-800, MLC-1000 and MLC-1200, respectively. MLC-800 exhibits the highest specific capacitance, consistent with its largest CV area and longest GCD discharge duration. Fig. 5c displays EIS curves featuring depressed semicircles and steep linear regions, indicating efficient charge transfer and nearly ideal capacitive behavior[60–63]. The rate-dependent performance of MLC-800 unveils a gradual decline in capacitance with escalating scan rates and current density (Fig. 5d and 5e). This phenomenon is ascribed to constrained ion accessibility at elevated polarization rates[64]. As indicated in Fig. 5f, an enhancement in current density from 0.5 to 10 A g^{-1} is observed, resulting in a decline in specific capacitance from 186.9 to 142.5 F g^{-1}. Notably, this decline exhibits a retention of 76.2% of its initial value, indicative of its effective rate capability.

Photo-assisted electrochemical measurements of MLC-800 were performed under xenon lamp illumination (Fig. 6a and 6b). Both the CV area and GCD duration increased under illumination compared with the conventional dark condition. As demonstrated in Fig. 6c, the specific capacitance exhibited a decline from 253.5 to 212.2 F g^{-1} as the current density in-

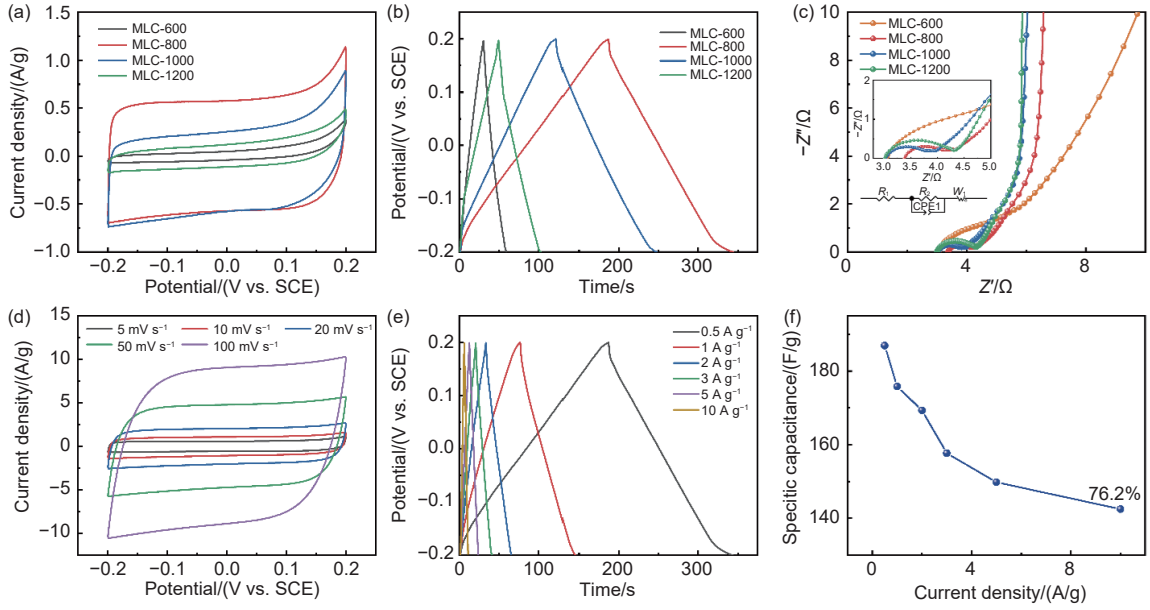

Fig. 5 (a) CV curves, (b) GCD curves and (c) EIS curves of Moiré-like lignin carbon. (d) CV and (e) GCD curves of MLC-800 under dark conditions. (f) Specific capacitance of MLC-800 under dark condition

creased from 0.5 A g^{-1}, retaining 83.7% of its initial value. This outcome surpasses the level observed under dark conditions, thereby substantiating the augmented rate capability under illumination. This improvement arises from photo-generated charge carriers that accelerate charge-transfer kinetics and suppress parasitic reactions[27]. A direct comparison in Fig. 6d and 6e shows that, under illumination, the CV curve encloses a larger area, while the GCD profile displays an extended charge–discharge duration. The specific capacitance of MLC-800 exhibited a substantial augmentation from 186.9 F g^{-1} in a state of darkness to 253.5 F g^{-1} under illumination, signifying a 35.6% enhancement. This observation underscores the pivotal role of light in augmenting the capacitive performance of the material.

To compare the morphological and optical effects, a non-Moiré reference sample (LC-800) was synthesized. Under dark conditions (Fig. 6f and 6g), the Moiré-like sample exhibits slightly larger CV areas and longer GCD durations, likely resulting from microfluidic effects that enhance electrolyte diffusion. At a current density of 0.5 A g^{-1}, the Moiré structure increases the specific capacitance from 172.5 to 186.9 F g^{-1}, corresponding to a 7.7% improvement. Under illumination (Fig. 6h and 6i), MLC-800 exhibits significantly enhanced performance, with its specific capacitance increasing from 214.4 to 253.5 F g^{-1}, representing a 15.4% enhancement. These findings confirm that the Moiré-like morphology enhances light harvesting, promotes charge generation and migration, and ultimately improves capacitive energy storage[40].

A symmetrical electric double-layer supercapacitor was fabricated to assess the practical applicability of an electrode with a Moiré-like structure, incor-

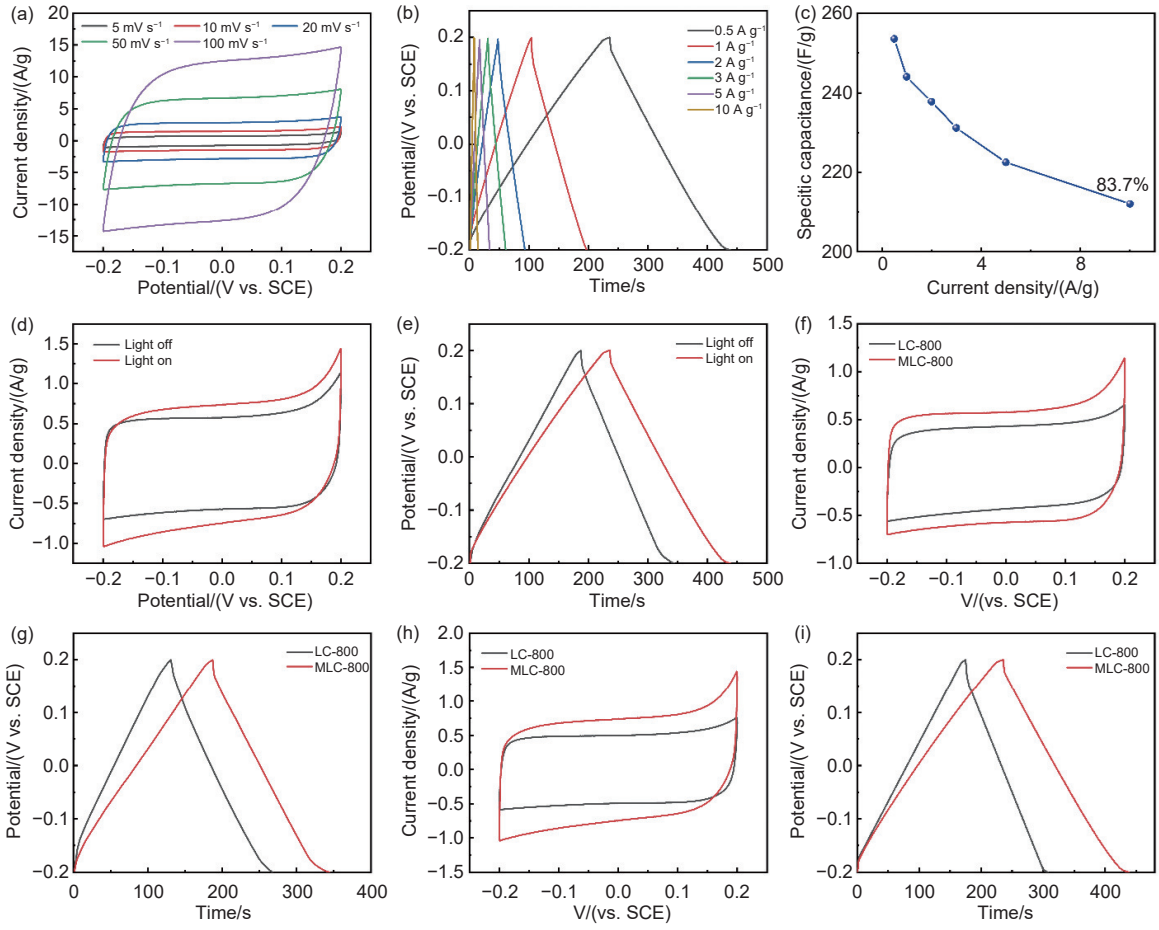

Fig. 6 (a) CV curves, (b) GCD curves and (c) specific capacitance of MLC-800 under illumination, (d) CV and (e) GCD curves of MLC-800 under dark and illumination. (f) CV and (g) GCD curves of MLC-800 and LC-800 under dark conditions. (h) CV and (i) GCD curves of MLC-800 and LC-800 under illumination

porating MLC-800 as the active material, FTO conductive glass as the current collector, a qualitative filter paper separator, and a PVA/H_2SO_4 gel electrolyte. The working mechanisms under both light and non-light conditions are schematically represented in Fig. 7. As is well established in the relevant literature, the charge-discharge mechanism operates through reversible adsorption and desorption of electrolyte ions at the porous electrode surface. The establishment of an electric double layer thus allows for energy storage. During the charging phase, under simultaneous light irradiation and an applied electric field, cations and anions migrate to the negative and positive electrodes, respectively, where they undergo physical adsorption onto the porous electrode surfaces. This process forms an electric double layer that stores energy electrostatically. Upon being discharged, the accumulated electrostatic potential is responsible for driving electron flow through an external circuit from a negative to a positive electrode. This process results in the delivery of electrical work. Concurrently, the adsorbed ions desorb from the surfaces of the electrodes and diffuse back into the electrolyte. As shown in Fig. 7c, under light irradiation, the Moiré-like structured electrode effectively prolongs the optical path length through multiple scattering and light trapping effects, thereby enhancing local light absorption at the electrode surface. The increased photon-electrode interaction promotes the generation and separation of photoinduced charge carriers, leading to a higher concentration of mobile cations and anions in the interfacial region. This enhanced ion availability facilitates charge accumulation at the electrode-electrolyte interface, ultimately contributing to the improved capacitive performance of the supercapacitor.

Fig. 8a compares the CV curves of the device recorded at a scan rate of 50 mV s^{-1} under dark and illuminated conditions. Under illumination, the CV profile approaches a more ideal rectangular shape with a significantly larger enclosed area, indicating enhanced capacitive behavior and greater charge-storage capacity. This enhancement is attributed to photogenerated charge carriers within the electrode, which reduce internal resistance and facilitate charge transfer during cycling. Consistent results are observed in the GCD curves (Fig. 8b). Fig. 8c displays GCD curves under illumination across a range of current densities (0.6–1.8 mA cm^{-2}). All profiles exhibit

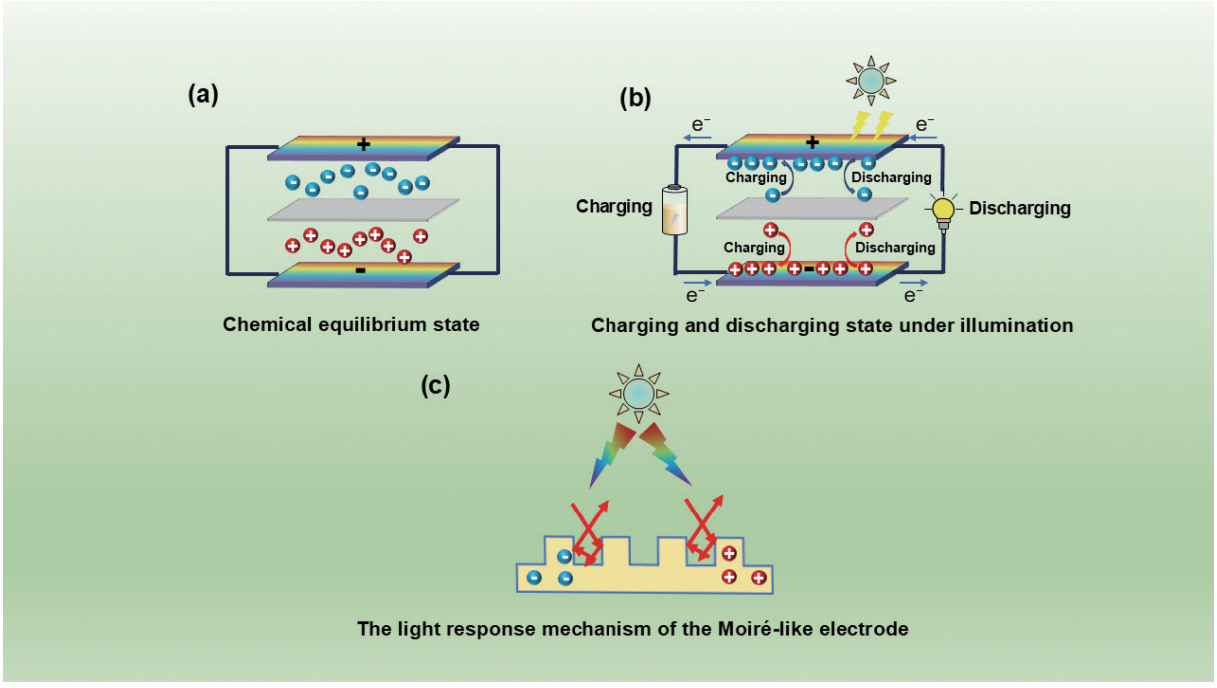

Fig. 7 Schematic representation of the working mechanism of PASC. (a) Chemical equilibrium state, (b) charging and discharging state under illumination. (c) The light response mechanism of the Moiré-like electrode

nearly symmetric triangular shapes, indicating good electrochemical reversibility and stable capacitive performance. The corresponding areal capacitances, calculated using Formula S2, are 58.84, 53.85, 49.76, 46.23, 43.22, 41.46 and 39.35 mF cm^{-2}, retaining 66.7% of the initial value at the highest current density. As summarized in Fig. 8e, the device exhibits higher capacitance and better retention under illumination than under dark conditions across all tested rates, highlighting the positive effect of light on enhancing capacitive properties. EIS was conducted to probe charge-transport characteristics (Fig. 8d). The Nyquist plot exhibits a small semicircle in the high-frequency region and an almost vertical line in the low-frequency domain, indicating minimal charge-transfer resistance and effective ion diffusion. These features confirm the device's superior capacitive characteristics and expeditious charge-transfer dynamics. The stability of the cycling process was evaluated over 5000 consecutive charge–discharge cycles at a current density of 5 mA cm^{-2} (Fig. 8f). The supercapacitor exhibited excellent long-term durability, with 85.2% of its initial capacitance being retained, whilst maintaining stable Coulombic efficiency. Formulas S3 and S4 were used to calculate energy and power densities, the maximum energy density recorded was 4.46 Wh kg^{-1}, attained at a power density of 365.2 W kg^{-1}. Notwithstanding the device's capacity of 1000 W kg^{-1}, it exhibited a noteworthy energy-power ratio of 2.96 Wh kg^{-1}, signifying a favorable energy-power balance. As demonstrated in the Ragone plot (Fig. S6), the device exhibits superior energy and power densities in comparison to multiple previously documented systems. This observation lends further credence to the notion that MLC-800 possesses considerable promise for utilization in high-performance energy storage applications[40,65–66].

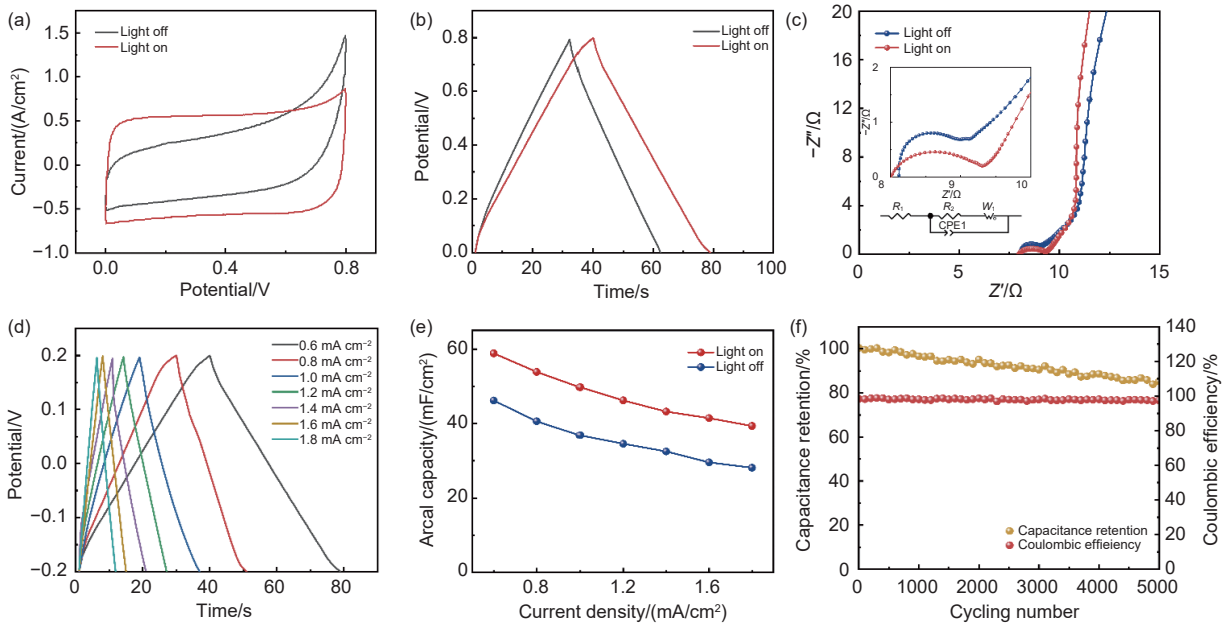

Fig. 8 (a) CV, (b) GCD and (c) EIS curves of symmetric supercapacitor under dark and illumination. (d) GCD curves of symmetric supercapacitor under illumination. (e) Areal capacity vs. current density under dark and illumination. (f) Cycle stability performance of symmetric supercapacitor

4 Conclusion

In summary, the present study proposes a novel methodology for the cost-effective and large-scale fabrication of Moiré-like lignin carbon architectures, utilizing readily available DVDs as templates through a synergistic templating-replication and high-temperature carbonization process. The resulting hierarchical architecture enhances light harvesting, prolongs photon propagation, and accelerates electrolyte diffusion both along the electrode surface and within the bulk structure, collectively delivering superior photo-

responsive capacitive behavior. Notably, the optimized MLC-800 electrode achieves a specific capacitance of 253.5 F g^{-1} at 0.5 A g^{-1} under illumination, corresponding to a 15.4% improvement over the non-Moiré counterpart, highlighting the strong coupling between optical modulation and charge-storage processes. When integrated into a symmetric solid-state supercapacitor with a PVA/H_2SO_4 gel electrolyte and filter paper separator, the device delivers an energy density of 4.46 Wh kg^{-1} at 365.2 W kg^{-1} and maintains 2.96 Wh kg^{-1} even at 1000 W kg^{-1} under illumination, underscoring its outstanding energy–power balance and operational stability. Overall, these findings provide compelling experimental evidence that Moiré-engineered optical architectures can substantially enhance photo-assisted charge storage. The present work proposes a new theoretical framework for integrating photonic design with carbon-based nanostructures, thereby establishing a foundation for the development of next-generation, high-performance photoelectrochemical energy-storage systems.

Acknowledgements

This work was supported by the Natural Science Foundation of China (52203352 and 52503392), Heilongjiang Province Key Research and Development Plan guidance project (GZ20210149), and Natural Science Foundation of Hebei Province (E2023202141).

References

[1] Ruben V, Brecht D, Kris M, et al. Lignin biosynthesis and structure[J]. Plant physiology, 2010, 153(3): 895-905.

[2] Wang S, Dai G, Yang H, et al. Lignocellulosic biomass pyrolysis mechanism: A state-of-the-art review[J]. Progress in Energy and Combustion Science, 2017, 62: 33-86.

[3] Li C P, Wu Y Q, Gao L X, et al. Lignin-derived carbon nanofibers with the micro-cracking structure for high-performance capacitive deionization[J]. Journal of Environmental Chemical Engineering, 2022, 10(6): 108952.

[4] Cui L, Cheng C, Peng F, et al. A ternary MnO_2-deposited RGO/lignin-based porous carbon composite electrode for flexible supercapacitor applications[J]. New Journal of Chemistry, 2019, 43: 14084-14092.

[5] José G M., Ramiro R R, Rosas M J, et al. Activation of electrospun lignin-based carbon fibers and their performance as self-standing supercapacitor electrodes[J]. Separation and Purification Technology, 2020, 241: 116724.

[6] Feng S, Fan Q, Ouyang Q, et al. Morphology and structure control of lignin-derived hierarchical porous carbon for high-performance supercapacitors[J]. Colloids and Surfaces A: Physicochemical and Engineering Aspects, 2024, 685: 133292.

[7] Jiang S Y, Yu X, Han L T, et al. Preparation and electrocatalytic hydrogen evolution properties of lignin-derived cabon/Ni/NiO composites[J]. International Journal of Electrochemical Science, 2021, 16(10): 211014.

[8] Tong W, Liang X, Huang F, et al. Preparation of activated carbon from paper black liquor lignin as high-performance electrode material[J]. European Journal of Wood and Wood Products, 2023, 82(3): 861-870.

[9] Ujwala A, Jaywant P, Jakob N, et al. Effect of sulfonation level on lignin/carbon composite electrodes for large-scale organic batteries[J]. ACS Sustainable Chemistry & Engineering, 2020, 8(49): 17933-17944.

[10] Xi Y B, Liu X, Xiong W L, et al. Converting amorphous kraft lignin to hollow carbon shell frameworks as electrode materials for lithium-ion batteries and supercapacitors[J]. Industrial Crops & Products, 2021, 174(15): 114184.

[11] Zhong W, Zheng J, Li P H, et al. Nickel-coordinated lignin enabled by nitrogen: A novel approach to high-performance carbon electrodes for supercapacitors[J]. Chemical Engineering Journal, 2025, 516: 164034-164034.

[12] Zhong X Y, Luo R M, Tan B B, et al. B-doped porous lignin carbon/copper-iron layered double hydroxides catalysts achieve roxarsine decontamination via photocatalytic oxalate activation[J]. Vacuum, 2025, 242: 114767.

[13] Zhang L M, You T T, Zhou T, et al. Interconnected hierarchical porous carbon from lignin-derived byproducts of bioethanol production for ultra-high performance supercapacitors[J]. ACS applied materials & interfaces, 2016, 8(22): 13918-13925.

[14] Zhang B H, Jia B B, Yan C, et al. Breaking the structural anisotropy of ZnO enables dendrite-free lithium-metal anode with ultra-long cycling lifespan[J]. Cell Reports Physical Science, 2022, 3(12): 101164.

[15] Arif M, Yang H R, Jiang Y, et al. Construction of three-dimensional $NiCo_2S_4$@Cu_2O nanowires with a high surface photovoltage to promote the energy efficiency of photo-assisted supercapacitors[J]. Journal of colloid and interface science, 2025, 698: 138067.

[16] Ch. B N, Paramane A, Randive R P. Effect of layered electrode on internal short circuit behaviour of Li-ion battery[J]. Journal of The Electrochemical Society, 2025, 172(9): 090536

[17] Li H J, Wang M M, Qi G H, et al. Oriented bacteriorhodopsin/polyaniline hybrid bio-nanofilms as photo-assisted electrodes for high performance supercapacitors[J]. Journal of Materials Chemistry A, 2020, 8(17): 8268-8272.

[18] Liu Y Y, Wang N, Li W X, et al. Synthesis of GN/MnO_2 nanocomposite materials for photo-assisted supercapacitor with enhanced capacities[J]. Journal of Science: Advanced Materials and Devices, 2024, 9(3): 100771.

[19] Li X R, Wang B, Lu F F, et al. A one-stone-two-birds strategy to lignin-derived porous carbon for supercapacitor electrodes[J]. Diamond & Related Materials, 2024, 142: 110831.

[20] Ma L, Zhao T C, Xu F, et al. A dual utilization strategy of lignosulfonate for MXene asymmetric supercapacitor with high area energy density[J]. Chemical Engineering Journal, 2021, 405: 126694.

[21] Renani S A, Hosseini Z, Eberhart D, et al. Photo-assisted symmetric and asymmetric supercapacitors based on molybdenum cobalt coated bismuth vanadate photoelectrodes: All-in-one energy harvesting and storage devices[J]. Journal of Power Sources, 2025, 640: 236687.

[22] Ito S, Sakai Y, Tsuji R, et al. Carbon-based multi-porous-layered-electrodes for highly-stable perovskite solar cells for space application[J]. Electrochemical Society Transactions, 2022, 109(1): 11.

[23] Tan Y D, Long Y F, Liu Z T, et al. 3D layer shape electrode of NiS in-situ growth on shaddock peel derived carbon for high-performance supercapacitors[J]. Journal of Electroanalytical Chemistry, 2025, 980: 118995.

[24] Yuan M, Zhou D S, Fan S N, et al. Efficient degradation of polystyrene microplastics in aquatic systems via plasma activated water: Mechanistic insights, life cycle assessment, and environmental safety evaluation[J]. Applied Catalysis B: Environment and Energy, 2026, 383: 126070.

[25] Huang J, Hu Y, Wang H, et al. Lignin isolated from poplar wood for porous carbons as electrode for high-energy renewable supercapacitor driven by lignin/deep eutectic solvent composite gel polymer electrolyte[J]. ACS Applied Energy Materials, 2022, 5(5): 6393-6400.

[26] Huang T, Zu X H, Ma J H, et al. High-yield production of porous carbon spheres derived from enzymatic hydrolysis lignin for zinc ion hybrid capacitors[J]. Frontiers of Chemical Science and Engineering, 2024, 18(2): 22.

[27] Mohamad M M, Hossein A M, Byeong-Kyu L. Effectiveness of MnO_2 and V_2O_5 deposition on light fostered supercapacitor performance of $WTiO_2$ nanotube: Novel electrodes for photo-assisted supercapacitors[J]. Chemical Engineering Journal, 2022, 450: 137941.

[28] Prasit P, Amornrat K, Husna H. Novel electrode composites of mixed bismuth-iron oxide/graphene utilizing for photo assisted supercapacitors[J]. Electrochimica Acta, 2021, 370: 137741.

[29] Hérou S, Bailey J J, Kok M, et al. High-density lignin-derived carbon nanofiber supercapacitors with enhanced volumetric energy density[J]. Advanced Science, 2021, 8(17): 2170109.

[30] Chen C, Ren T X, Lu J Q, et al. Precisely tuning the alkali metal content in lignosulfonate for understanding the pore structure evolution of its derived carbons enabling high areal capacitance microsupercapacitors[J]. Journal of Energy Storage, 2026, 141: 119477.

[31] Kim Y, Bark H, Gupta A, et al. Photo-switchable supercapacitors based on photo-responsive azopolymers: enabling dual-functionality in tunable high capacitance and low self-discharge[J]. Advanced Energy Materials, 2025, 15(13): 2405480.

[32] Zhang Z H, Zhu S Z. Design of frictionless interfaces for moiré layers[J]. Physical review letters, 2025, 135(11): 116202.

[33] Zhang X L, Long Y H, Lu N, et al. Moiré superlattice in two-dimensional materials: fundamentals, applications, and recent developments[J]. ACS applied materials & interfaces, 2024, 16(50): 68724-68748.

[34] Owjifard Z, Tavana A, Hosseini M. Critical current density enhancement in superconductor tapes using moiré pinning centers for device and power applications[J]. Journal of Alloys and Compounds, 2025, 1029: 180676.

[35] Park D, Park C, Yananose K, et al. Unconventional domain tessellations in moiré-of-moiré lattices[J]. Nature, 2025, 641(8064): 1-8.

[36] Hong R Z, Zhao X J, Lu R Y, et al. Fabrication of polypyrrole hollow nanospheres by hard-template method for supercapacitor electrode material[J]. Molecules, 2024, 29(10): 2331.

[37] Katarzyna T, Rafał O, Jędrzej K, et al. Modified mesoporous carbon material (Pb-N-CMK-3) obtained by a hard-templating route, dicyandiamide impregnation and electrochemical lead particles deposition as an electrode material for the u(vi) ultratrace determination[J]. Materials, 2021, 14(21): 6490.

[38] Li P, Niu Y F, Yang Q Y, et al. “Template-assisted synthesis” strategy to improve the bifunctional catalytic activity of oxygen electrode for reversible protonic ceramic electrochemical cell[J]. Ceramics International, 2024, 50(20): 40510-40517.

[39] Zhang Z Y, Hu H M, Yang J, et al. The application of porous

carbon derived from furfural residue as the electrode material in supercapacitors[J]. Polymers, 2024, 16(23): 3421.

[40] Cai H W, Li Y D, Liu D, et al. Construction of Moiré-like TiO_2/polypyrrole electrodes for high performance photo-assisted supercapacitors[J]. Colloids and Surfaces A: Physicochemical and Engineering Aspects, 2024, 703: 135386.

[41] Lai X Y, Li G H, Coe M A, et al. Moiré periodic and quasiperiodic crystals in heterostructures of twisted bilayer graphene on hexagonal boron nitride[J]. Nature materials, 2025, 24(7): 1-8.

[42] Nuckolls K. P, Yazdani A. A microscopic perspective on moiré materials[J]. Nature Reviews Materials, 2024, 9(7): 460-480.

[43] Gedara A S B, Rice S P, Evans E P, et al. Thermodynamic stability and site-specific distribution of graphitic and pyridinic nitrogen in graphene Moiré on Ru(0001)[J]. Advanced Materials Interfaces, 2025, 12(13): 2500142.

[44] Chen K S, Zhou W T, Feng Z, et al. Unlocking the potential of Moiré superlattices in electrocatalysis, photocatalysis, and piezo-photocatalysis[J]. Small, 2025, 21(22): 2503008.

[45] Li Y, Hua Y Q, Sun N, et al. Moiré superlattice engineering of two-dimensional materials for electrocatalytic hydrogen evolution reaction[J]. Nano Research, 2023, 16(7): 8712-8728.

[46] Belim V S, Tikhomirov V I. Monte carlo modeling of the graphene Moiré structure on an Ir(111) substrate[J]. Journal of Surface Investigation: X-ray, Synchrotron and Neutron Techniques, 2025, 19(3): 710-716.

[47] Lau C N, Bockrath M W, Mak K F, et al. Reproducibility in the fabrication and physics of moiré materials[J]. Nature, 2022, 602(7895): 41-50.

[48] Wang Y, Lan Y J, Song Q, et al. Colorful efficient Moiré-perovskite solar cells[J]. Advanced Materials, 2021, 33(15): 2008091.

[49] Arribas D, Coronado S A, Cirera B, et al. Moiré-induced enhanced hydrogen adsorption on graphene[J]. Small, 2025, 21(37): 07323.

[50] Li R Z, Zhou Y P, Li W B, et al. Structure engineering in biomass-derived carbon materials for electrochemical energy storage[J]. Research, 2020, 2020: 8685436.

[51] Xiao L F, Lu H Y, Fang Y J, et al. Low-defect and low-porosity hard carbon with high coulombic efficiency and high capacity for practical sodium ion battery anode[J]. Advanced Energy Materials, 2018, 8(20): 1703238.

[52] Zhu Y Y, Chen M M, Li Q, et al. High-yield humic acid-based hard carbons as promising anode materials for sodium-ion batteries[J]. Carbon, 2017, 123: 727-734.

[53] Lu S Y, Jin M, Zhang Y, et al. Chemically exfoliating biomass into a graphene-like porous active carbon with rational pore structure, good conductivity, and large surface area for high-performance supercapacitors[J]. Advanced Energy Materials, 2018, 8(11): 1702545.

[54] Gong Y N, Li D L, Luo C Z, et al. Highly porous graphitic biomass carbon as advanced electrode materials for supercapacitors[J]. Green Chemistry, 2017, 19(17): 4132-4140.

[55] Jyoti L K, Ajaikumar S, Päivi A M, et al. Efficient C—C coupling of bio-based furanics and carbonyl compounds to liquid hydrocarbon precursors over lignosulfonate derived acidic carbocatalysts[J]. Catalysis Science & Technology, 2018, 8(9): 2449-2459.

[56] Vali P I, Anusha B, Pruthvija M, et al. Bamboo and coconut shell based activated carbon: A Raman spectroscopic study[J]. Materials Chemistry and Physics, 2024, 318: 129240.

[57] Hou Z D, He W J, Wu F X, et al. Tuning π-π carbon restacking hindrance to remodify hard carbon crystallites for advanced sodium energy[J]. Energy Storage Materials, 2025, 80: 104455-104455.

[58] Liu F Y, Wang Z X, Zhang H T, et al. Nitrogen, oxygen and sulfur co-doped hierarchical porous carbons toward high-performance supercapacitors by direct pyrolysis of kraft lignin[J]. Carbon, 2019, 149: 105-116.

[59] Sundari S G, Arthi G, Raghu S, et al. Single step, direct pyrolysis assisted synthesis of nitrogen-doped porous carbon nanosheets derived from bamboo wood for high energy density asymmetric supercapacitor[J]. Journal of Energy Storage, 2021, 42: 103048.

[60] Liu D, Li Y D, Wang C Y, et al. Numerous active sites in self-supporting Co_3O_4 nanobelt array for boosted and stabilized 5-hydroxymethylfurfural electro-oxidation[J]. Applied Catalysis A, General, 2024, 669: 119497.

[61] Song M S, Xing Y S, Li Y D, et al. Fe and Cu double-doped Co_3O_4 nanorod with abundant oxygen vacancies: A high-rate electrocatalyst for tandem electroreduction of nitrate to ammonia[J]. Inorganic Chemistry, 2023, 62(40): 16641-16651.

[62] Wang J G, Yang Y, Huang Z H, et al. MnO_2/polypyrrole nanotubular composites: reactive template synthesis, characterization and application as superior electrode materials for high-performance supercapacitors[J]. Electrochimica Acta, 2014, 130: 642-649.

[63] Jiang M W, Zhao Y M, Hou Z D, et al. Leveraging sodium storage of water-deficient prussian blue analogues by deep eutectic chemistry[J]. ACS Energy Letters, 2025, 11(1): 526-536.

[64] Yang Z Y, Li Y D, Liu D, et al. Oxygen vacancy-regulated nanorod array electrodes for boosting the electrocatalytic synthesis of ammonia from nitrate wastewater[J]. Chemical communications, 2024, 60: 9950-9953.

[65] Popoola I K, Gondal M A, Popoola A, et al. Inorganic perovskite photo-assisted supercapacitor for single device energy harvesting and storage applications[J]. Journal of Energy Storage, 2023, 73: 108828.

[66] Zhang W L, Zhao M Z, Liu R Y, et al. Hierarchical porous carbon derived from lignin for high performance supercapacitor[J]. Colloids and Surfaces A: Physicochemical and Engineering Aspects, 2015, 484: 518-527.